A Stochastic Model for Studying the Laminar Structure of Cortex From MRI

Patrick Barta*, Michael I. Miller, *Senior Member, IEEE*, and Anqi Qiu

***Abstract*—The human cerebral cortex is a laminar structure about 3 mm thick, and is easily visualized with current magnetic resonance (MR) technology. The thickness of the cortex varies locally by region, and is likely to be influenced by such factors as development, disease and aging. Thus, accurate measurements of local cortical thickness are likely to be of interest to other researchers. We develop a parametric stochastic model relating the laminar structure of local regions of the cerebral cortex to MR image data. Parameters of the model include local thickness, and statistics describing white, gray and cerebrospinal fluid (CSF) image intensity values as a function of the normal distance from the center of a voxel to a local coordinate system anchored at the gray/white matter interface. Our fundamental data object, the intensity-distance histogram (IDH), is a two-dimensional (2-D) generalization of the conventional 1-D image intensity histogram, which indexes voxels not only by their intensity value, but also by their normal distance to the gray/white interface. We model the IDH empirically as a marked Poisson process with marking process a Gaussian random field model of image intensity indexed against normal distance. In this paper, we relate the parameters of the IDH model to the local geometry of the cortex. A maximum-likelihood framework estimates the parameters of the model from the data. Here, we show estimates of these parameters for 10 volumes in the posterior cingulate, and 6 volumes in the anterior and posterior banks of the central sulcus. The accuracy of the estimates is quantified via Cramer-Rao bounds. We believe that this relatively crude model can be extended in a straightforward fashion to other biologically and theoretically interesting problems such as segmentation, surface area estimation, and estimating the thickness distribution in a variety of biologically relevant contexts.**

***Index Terms*—Cortical thickness, intensity-distance histogram (IDH), normal distance, partial volume effect.**

I. Introduction

HIGH-RESOLUTION magnetic resonance (MR) imaging affords an opportunity to acquire detailed information about human neuroanatomy in living subjects. One major challenge in using MR data in brain studies relates to the problem of extracting biologically relevant features from the MR images. Among the most informative of these features are the boundaries of anatomical regions of interest. Some regions of the brain, such as the deep nuclei, thalamus, hippocampus, and ventricles, are easily conceptualized as three-dimensional (3-D) submanifolds (subvolumes) because of their clear-cut tissue boundaries. A natural coordinate system for those parts of the brain that can be most easily understood as 3-D submanifolds is the 3-D lattice coordinate system based on voxel locations.

By contrast, the cerebral cortex is a thin laminar structure about 3 mm in thickness with a large surface area on the order of 1.3×10^5 mm^2 [1] for both hemispheres. Although the cortex can be conceptualized as a 3-D submanifold too, it is meaningful to think of it as a 2-D submanifold, a part of the brain more like a surface than a volume. Conventional boundaries of cortical regions are typically based on sulcal-gyral patterns, geometric features defined intrinsically with respect to the surface coordinates associated with the convolutions of the cortex, rather than extrinsically via the interface between the different kinds of tissues. The boundaries of the occipital lobe, for example, is defined by sulci, not by a boundary between gray and white matter. For these reasons, Van Essen and others have argued for the introduction of a second, local, 2-D coordinate system which is intrinsic to the cortical surface in the region of some particular gyrus [2]–[4].

Researchers have developed many methods for generating these 2-D local coordinate systems on the cortical surface. Most of these methods are based on statistical decision theory [3]–[22]. Many proposed 2-D surface coordinate systems on the cortex describe its convoluted geometry via bijective diffeomorphisms on local 2-D Euclidean charts [8], [23]–[31].

Studies of the cortical mantle as a laminar structure have shown specific morphometric changes in several neuropsychiatric disorders, including schizophrenia, Alzheimer's, Huntington's diseases [2], [32]–[38]. Changes in the structure of the cerebral cortex have been associated with both Alzheimer's disease (AD) and healthy aging [2], [39], [40].

This paper examines the properties of a new statistical model relating the laminar structure of the neocortical mantle to the measured magnetic resonance imaging (MRI) data as a function of the set distance of a voxel's center to the local coordinates of the 2-D submanifold at the gray/white matter interface. The construction of the local normal coordinate system is based on the constructed orthogonal frame consisting of the two axes spanning the tangent plane to the gray/white matter interface, and the associated third normal axis measuring the relative normal distance from the this interface to the center of individual voxels.

Manuscript received November 30, 2004; revised February 16, 2005. This work was supported in part by the National Institutes of Health (NIH) under Grant 1 P41 RR15241-01A1, Grant 1 R01 EB00975-01, Grant 1 R01 MH064838, and Grant R01 MH60590. The Associate Editor responsible for coordinating the review of this paper and recommending its publication was C. Davatzikos. *Asterisk indicates corresponding author.*

*P. Barta is with the Center for Imaging Science and the Department of Biomedical Engineering, The Johns Hopkins University, Clark Hall 301, 3400 N. Charles Street, Baltimore, MD 21218 USA. He is also with the Department of Psychiatry, The Johns Hopkins University School of Medicine, Baltimore, MD 21205 USA (e-mail: patr@jhmi.edu).

M. I. Miller is with the Center for Imaging Science and the Department of Biomedical Engineering, The Johns Hopkins University, Baltimore, MD 21218 USA.

A. Qiu is with the Center for Imaging Science and the Department of Electrical and Computer Engineering, The Johns Hopkins University, Baltimore, MD 21218 USA.

Digital Object Identifier 10.1109/TMI.2005.846861

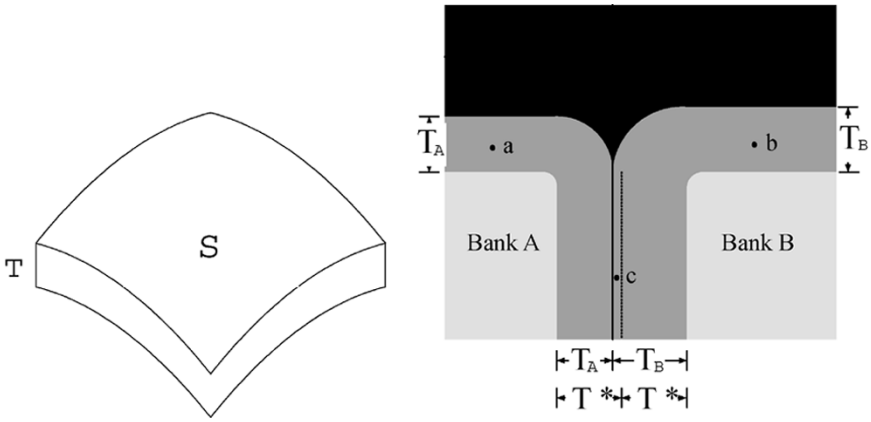

Fig. 1. Laminar approximation. The left panel shows the laminar approximation where S denotes the cortical surface and T the cortical thickness. The right panel shows a sulcus with two banks A, B with thickness T_A, T_B, respectively; the summed thickness is denoted $T^\star = (T_A + T_B)/2$. Points "a" and "b" are located in bank A and bank B, respectively. Point "c", anatomically associated with bank B, is assigned by the set distance calculation to bank A.

The intrinsic columnar structure of the cortex lies roughly perpendicular to the gray/white surface. The cortical thickness has been measured by the following algorithms: distance of corresponding point on inner and outer gray matter surfaces following the surface expansion [13], distance along the surface normal [13], an iteratively computed surface normal, shortest distance between inner and outer surfaces [41]. In this paper, we define the cortical thickness as normal distance relative to the gray/white matter interface.

We augment the standard MRI image indexed over the regular lattice of voxels $I(x_k)$, $k = 1, 2, \ldots$ with the secondary local normal distance coordinates labeling each voxel x_k with its distance D in normal coordinates to the gray/white matter interface as basic data structure—image-distance histogram (IDH), a direct generalization of the conventional histogram. We model the voxel intensity values in the MRI image as a conditionally Gaussian random field with mean and covariance parameterized by the set distance from the voxel's center to the manifold. Such a statistical model then relates the gross parameters of the cortical mantle (e.g., thickness and surface area) to the measured image data as well as to the mean and variance of the intensity for each tissue compartment. This allows for the direct estimation via maximum-likelihood of these gross parameters from data obtained from MR images. Our basic insight recognizes that tissue properties change as a function of the normal distance from the local coordinates. By generating a probability law indexed by this normal distance, the laminar structure parameters can be estimated. Such an approach provides an opportunity to greatly increase the power of the estimation of the geometric parameters for local cortical regions. Furthermore, the calculations we propose entirely avoid the problem of trying to identify the border between gray matter and cerebrospinal fluid (CSF), a problem which we argue is poorly posed because of intrinsic cortical geometry.

II. The Laminar Cortex Model

We begin with the *laminar approximation* depicted in the left panel of Fig. 1. The laminar approximation is the observation that the volume of a thin laminar structure is approximately its surface area times its length. The right panel of Fig. 1 shows a small cross section through a cortical sulcus. Cortical thicknesses on opposite banks of the sulcus need not be identical, and we label these thicknesses as T_A and T_B. In the region of the central sulcus, for example, von Economo [42] states that the cortical thickness of the sensory cortex is less than 2 mm, while the thickness of the motor cortex, which is on the other side of the sulcus, is 3.2–3.5 mm. In the following, we use T_A and T_B to distinguish between the cortex on opposite sides of a sulcus, and T when we are not concerned with this distinction.

The right panel of Fig. 1 shows how two anatomically meaningful 2-D manifolds appear, one at the boundary of gray and white matter, the other at the boundary of gray matter and CSF. Some of the exterior surface of gray matter is contiguous with CSF, some is contiguous with the gray matter on the other side of the sulcus. In general, the gray/white matter boundary manifold is geometrically better behaved than the gray-matter/CSF manifold because it does not appear to intersect itself as it sometimes does in MRI images We call regions of the cortex where the exterior boundaries of two different gyri touch "hidden," and places where they do not touch "exposed". We note that our term "hidden" is not equivalent to another common term, "buried"—meaning within the depth of a sulcus—because there may be CSF within a buried sulcus, and the exterior boundaries of two different gyri within a sulcus are not hidden when there is a gray-matter/CSF boundary. We use the subscripts x and h in calculations relating to the exposed and hidden cortex, respectively.

The right panel of Fig. 1 shows how tissue properties vary as a function of distance to the local coordinates. Image voxels $I(x_k)$ with negative normal distance D should be white matter, positive distance $0 < D \leq T$ gray matter, and $D > T$ cerebrospinal fluid. Moreover, examining Fig. 1 carefully illustrates another essential characteristic of hidden cortex. For sulcal banks which are hidden, there is essentially no identifiable CSF, and the gray/CSF boundary is absent.

Of course, because of the convoluted nature of the cortex, this understanding of how tissue properties vary as a function of distance to the local coordinates is oversimplified. For example, inside the Sylvian fissure, we could conceivably traverse from the temporal gyrus through the CSF of the Sylvian fissure, and

into a gyrus in the frontal or parietal lobe. For the purposes of analysis here, we minimize such problems by limiting our analysis to voxels whose distance from the gray/white manifold lies within 2–3 mm of a rough estimate of the thickness. (This rough estimate can be easily obtained by inspecting the MRI data and the number of voxels that span the cortex.)

A. Normal Coordinates

The location of voxels in the cortex can be described both with respect to the usual coordinate system with coordinate values $x_k \in X \subset \mathbb{R}^3$, $k = 1,2,\ldots$ representing a regular cubic lattice of voxel locations or with respect to a second local coordinate system relative to the gray/white boundary. This second local coordinate system is associated with a tangent space $T(s)$, $s \in S(\triangle)$ to the submanifold defined by the gray/white boundary. If we model the gray/white surface in the continuum as a 2-D differentiable submanifold $S \subset \mathbb{R}^3$ with tangent space at each of its points T_s, $s \in S$, we can assume that this interface is a smooth 2-D surface with the property that for each point $s \in S$ there exists a patch containing s with smooth correspondence to the plane (1-1, onto, differentiable). The particular local coordinate systems which we use to understand patches of the cortical surface are defined in terms of the orthogonal frame positioned at the tangent plane of the manifold. Define the partial derivative notation of a function of two variables $f(u,v)$ as $f_u = \partial f/\partial u$, $f_v = \partial f/\partial v$. Define the orthonormal tangent vectors spanning the tangent plane T_s at s as E_{1s}, E_{2s}; complete the orthogonal frame via E_{3s}. Then the surface is defined locally around s by

$$x(u,v) = s + uE_{1s} + vE_{2s} + E_{3s}f(u,v), \quad u,v \in D \subset \mathbb{R}^2. \tag{1}$$

This coordinate system is rooted at $x(0,0) = s$. It is local in the sense that $x(D) \subset S$ will not in general be the entire surface. Take, for example, two gyri which curve back on each other. It is necessary to choose several patches which intersect and for which projecting onto the plane of the tangent provides a local bijective correspondence. The orthogonal frame over the entire local patch of coordinates have tangent vectors

$$T_{1x(u,v)} = \frac{\partial x(u,v)}{\partial u} = E_{1s} + E_{3s}f_u(u,v) \tag{2}$$

$$T_{2x(u,v)} = \frac{\partial x(u,v)}{\partial v} = E_{2s} + E_{3s}f_v(u,v) \tag{3}$$

with surface normal given by the cross-product

$$N_{x(u,v)} = \frac{-f_uE_{1s} - f_vE_{2s} + E_{3s}}{\sqrt{1+f_u^2+f_v^2}}. \tag{4}$$

The normal axis $N_{x(u,v)}$, is normal to every point in the smooth local coordinate representation $x(u,v) \in x(D) \subset S(\triangle)$. We measure distance D by the coordinate along this normal axis.

We begin by fitting an initial surface manifold of the gray/white boundary with reference the local statistics of the MRI intensity values using the expectation-maximization algorithm [7], [10] and generating an isosurface [3], [4], [43] over a manifold whose extent is greater than the anatomical structure of interest so that the entire structure of interest in contained within this larger manifold. From any point on the surface $s \in S(\triangle)$ there are a continuum of points in the volume which are at minimum distance d measured along the axis N_s. Along these normal axes are points which minimize the set distance function $D : x_k \in X \mapsto D(x_k) \in [\min, \max]$ from the point $x_k \in X$ to the closest point in $S(\triangle)$

$$D(x_k) = \min_{s \in S(\triangle)} \|x_k - s\|. \tag{5}$$

Positive distance values $D > 0$ are taken as relative to the outward-pointing normal of the cortex (toward the skull), while negative values correspond to displacements toward the deep brain nuclei. We manually identify a submanifold corresponding to the anatomical structure of interest within the initial manifold. We then analyze only those voxels who are thus associated with this anatomic submanifold to avoid errors where voxels near the boundaries of the submanifold would have been improperly assigned to the submanifold rather than to the manifold corresponding to the difference between the initial coarse manifold and the manifold associated with the structure of interest.

This ancillary local coordinate system of the gray/white boundary manifold associates with the MRI volume voxel values real numbers representing the shortest distance from the voxel's center (in the regular 3-D lattice) to the triangulated graph of the manifold derived from the gray/white boundary. For all applications the closest points lying along the normal are found using the distance calculation algorithm described in [3], [4], [44].

We cannot readily distinguish between T_A and T_B in the hidden cortex because of the lack of CSF. As shown in the right panel of Fig. 1, point "c," which is anatomically related to bank B, is associated with bank A by the set distance calculation. In the following, we define $T^* = (T_A + T_B)/2$, the average of T_A and T_B, because it is easier to understand the association of voxel's set distance with regard to this value. Obviously, T^* determines which gyrus a voxel in the hidden cortex will be associated with.

Fig. 2 illustrates our method for generating the distance maps for regions of interest. The region of interest (ROI) volume is shown in Fig. 2(a). Using isocontouring, [10], [21], the triangulated mesh $S_\triangle$ is generated as in Fig. 2(b). By dynamic programming generation of boundaries of local submanifolds [44], the region of interest on the 2-D manifold S_{ROI} is shown as a red line in the section plane shown in Fig. 2(b), where S_{ROI} is extracted from as shown in Fig. 2(c). The distance map is calculated computing the set distance between every voxel in the volume and the manifold. Fig. 2(d) shows the set distance map for the same slice as in Fig. 2(a); green and blue denote positive (gray matter) and negative (white matter) distances, respectively.

III. A Marked Poisson Process Model of the Intensity-Distance Histogram

A. The MR Image as Marked Poisson Process

We augment the MR image intensities $I(x_k)$, $k = 1,2,\ldots$ by the normal distance calculated at each voxel, $(I,D)(x_k)$, $k = 1,2,\ldots$, where $(I,D) : X \to \mathbb{R} \times \mathbb{R}$ consists of the image value and the distance to the cortical manifold. We call this joint data structure as the MRI-distance map or MRID map.

Our stochastic model for the MRID map is that of a marked-filtered Poisson process [45]. For any given normal distance D, we assume that the intensity of occurrence of voxels (gray, white

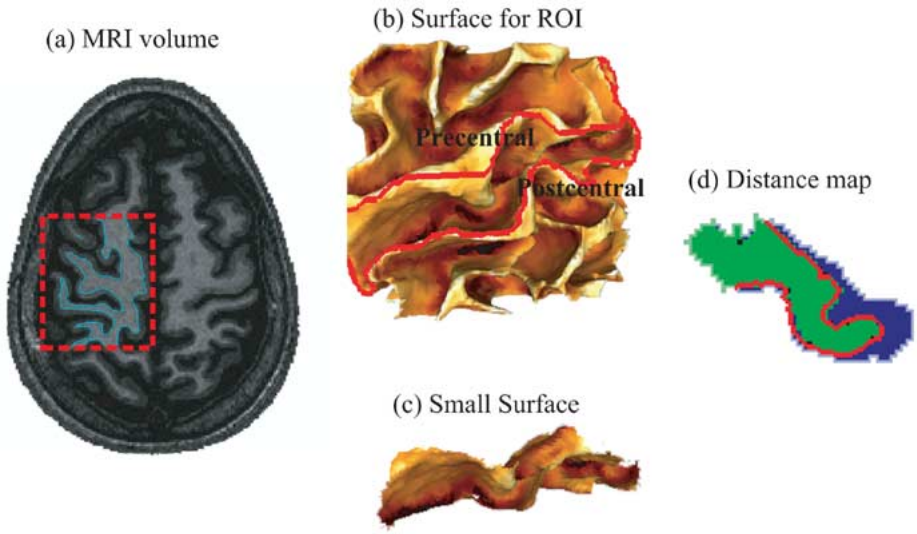

Fig. 2. Identification of region of interest and distance map calculation. (a) MRI volume; the volume in the red frame is defined as region of interest. (b) Isocontoured surface. The region marked by red line depicts the two banks of the central sulcus on the surface which were extracted from. (c) Small surface associated with the central sulcus. (d) Distance map containing the voxels in the ROI that are the closest to the surface shown in (c). Green and blue regions correspond to positive and negative distances, respectively.

or CSF) is a marked-Poisson arrival process with rate $\lambda(D)$. Brain tissue is marked with the image intensity values, and we assume that the gray, white, and CSF voxel intensities follow a family of probability law with densities $f(\cdot; D)$ indexed by the normal distance from the manifold. The IDH process is thus just a marked Poisson arrival process with intensity

$$\lambda(I, D) = f(I; D)\lambda(D). \tag{6}$$

We chose this arrival process primarily because it fits our data fairly well, and the theory of such processes is simple and well understood.

B. Gaussian Random Field for Voxel Measurements

We further assume throughout the image intensity field is an uncorrelated Gaussian random field (diagonal covariance) with mean and variance $\mu(D), \sigma(D), D \in [min, max]$, values determined by the tissue type and distance from the cortical surface. The marking process of the IDH thus has density

$$f(I; D) = \frac{1}{\sqrt{2\pi\sigma^2(D)}} e^{-\frac{(I-\mu(D))^2}{2\sigma^2(D)}}. \tag{7}$$

Just as in our choice of arrival process, we chose this form for the marking process primarily because of its simplicity.

We now consider the two distinct geometric circumstances determining means and variances which occur in modeling the laminar structure of the human brain, associated with the exposed and hidden cortex.

Exposed Cortex: For exposed cortex we assume that the arrival process rate for voxels, regardless of value, is a constant, with mean and variance profiles for the marking process

$$\begin{aligned}\mu_x(D) &= \mu_w \cdot U(-D) + \mu_g \cdot [U(D) - U(D-T)] \\ &\quad + \mu_c \cdot U(D-T) \qquad (8)\\ \sigma_x^2(D) &= \sigma_w^2 \cdot U(-D) + \sigma_g^2 \cdot [U(D) - U(D-T)] \\ &\quad + \sigma_c^2 \cdot U(D-T) \qquad (9)\end{aligned}$$

where μ_w, μ_g, μ_c, the means for white, gray and CSF, and similarly for the standard deviations σ_w, σ_g, σ_c, and $U(x) = 1$ if $x \geq 0$, 0 otherwise.

Fig. 3 illustrates the geometry of the section of exposed cortex; (a) shows the results of a simulation with typical values for dependent parameters $\mu_w = 120$, $\mu_g = 90$, $\mu_c = 30$, $\sigma_w = 20$, $\sigma_g = 15$, $\sigma_c = 10$, and $T = 3$ mm.

Because cortex is not much thicker than the size of the voxels in an MR image, there is considerable blurring of the edges of the cortex, and we must take this "partial volume" artifact into account. In MRI the voxel resolution is determined by the distribution of phases across a voxel; the resulting voxel intensity resolution corresponds to twice the full-width at half-maximum of the $sinc$ function [46], [47] if we assume that the voxel size corresponds to sampling at the Nyquist rate. We model this partial volume effect $sinc$ function of MRI data by the convolution of the ideal intensity profile with a Gaussian density function having zero mean and constant standard deviation σ_v. For any particular value for distance $D = d$, the density $f(\cdot; d)$ is thus a linear combination of Gaussian random variables (and, hence, Gaussian) with mean given by the convolution of this Gaussian point spread function with the mean. Defining the function $P(D; \sigma_v^2) = \int_{-\infty}^{D} (e^{-x^2/2\sigma_v^2}/\sqrt{2\pi}\sigma_v)dx$ gives the observed mean and variance of image intensity values corrected for partial volume effect as a function of D, which are

$$\mu_x(D) = \alpha_{xc}(D)\mu_c + \alpha_{xg}(D)\mu_g + \alpha_{xw}(D)\mu_w \tag{10}$$
$$\sigma_x^2(D) = \alpha_{xc}^2(D)\sigma_c^2 + \alpha_{xg}^2(D)\sigma_g^2 + \alpha_{xw}^2(D)\sigma_w^2 \tag{11}$$

with the weights

$$\begin{aligned}\alpha_{xc}(D) &= P\left(D - T; \sigma_v^2\right)\\ \alpha_{xg}(D) &= P\left(D; \sigma_v^2\right) - P\left(D - T; \sigma_v^2\right)\\ \alpha_{xw}(D) &= 1 - P\left(D; \sigma_v^2\right).\end{aligned}$$

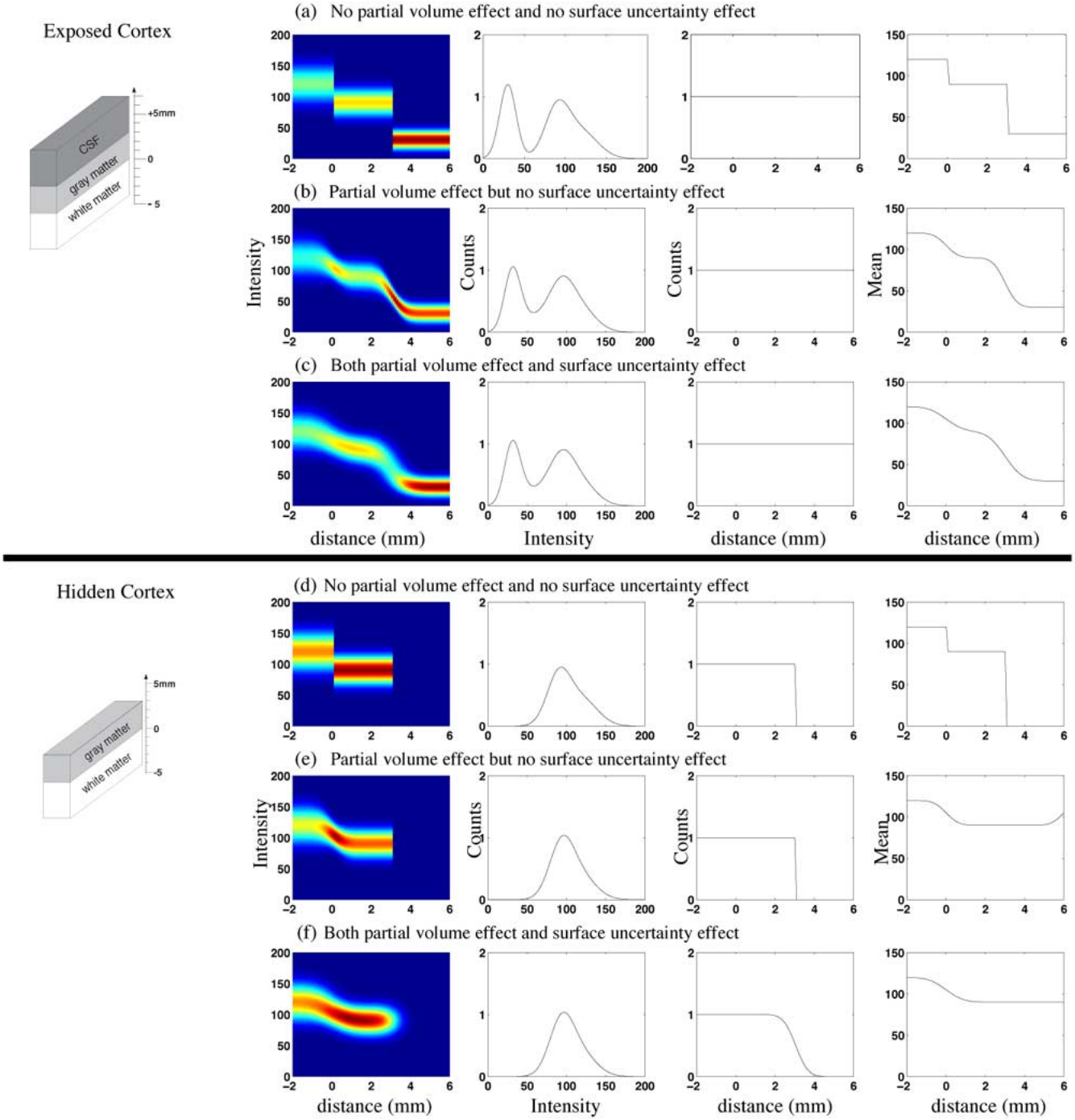

Fig. 3. IDH simulation. Column 1 illustrates geometric structures for exposed (top), hidden (bottom). Columns 2–5 show the intensity-distance histogram, intensity histogram, distance histogram and mean curve respectively. Rows (a, d) represent simulations without any effects, rows (b, e) with the effect of partial volume, rows (c, f) with effects of partial volume and surface uncertainty. Parameters are $T = 3$ mm, intensity parameters $\mu_c = 30, \mu_g = 90, \mu_w = 120$, and variances $\sigma_c^2 = 100, \sigma_g^2 = 225, \sigma_w^2 = 400$, voxel point-spread kernel $\sigma_v = 0.5$ mm, and surface uncertainty kernel $\sigma_u = 0.5$ mm.

Fig. 3(a), (b) shows the model means without and with this partial volume effect, respectively. Notice that as the result of the partial volume effect the mean values at a particular true distance for the cortex are no longer step functions. Fig. 3(b) depicts how the mean intensity now changes smoothly from white to gray and from gray to CSF as a function of distance. In the exposed cortex, mean intensity value at $D = 0$ mm is approximately equal to $1/2(\mu_w + \mu_g)$, dependent on value of σ_p, whereas at $D = T$ mean intensity is around $1/2(\mu_g + \mu_c)$.

We find that the profile of arrival rate for the CSF density is not uniform in density, and rather is monotonically decreasing as a linear or quadratic function. We attribute this to the nonuniform nature of the thickness of CSF as well as the nonuniform definition of the cortical subvolumes of the brain. Our first order models the arrival rate $\lambda(D)$ as a linear decreasing function with

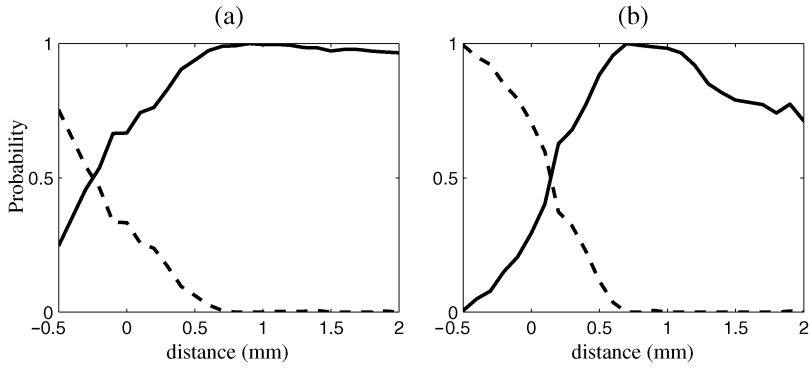

Fig. 4. Conditional probability. Conditional probability of occurrence of white (dashed line), and gray (solid line) compartments as a function of millimeter distance from the gray/white matter boundary. (a) Gray matter is assigned to the negative side of the origin (Brain: cs2). (b) White matter is assigned to the positive of the origin (Brain: cs1).

slope s; the parameter s is estimated for each subvolume for the exposed cortex.

Hidden Cortex: For the case of hidden cortex, there is no CSF between the hidden cortex and the arrival rate is 0 for normal distances greater than $T^\star$. We have

$$\mu_h(D) = \mu_w U(-D) + \mu_g \left[U(D) - U(D - T^\star)\right] \quad (12)$$
$$\sigma_h^2(D) = \sigma_w^2 U(-D) + \sigma_g^2 \left[U(D) - U(D - T^\star)\right]. \quad (13)$$

By taking the partial volume effect, the means and variances are as follows:

$$\mu_h(D) = \alpha_{hg}(D)\mu_g + \alpha_{hw}(D)\mu_w \quad (14)$$
$$\sigma_h^2(D) = \alpha_{hg}^2(D)\sigma_g^2 + \alpha_{hw}^2(D)\sigma_w^2 \quad (15)$$

with weights determined by the thickness $T^\star$

$$\alpha_{hg}(D) = P\left(D; \sigma_v^2\right) - P\left(D - 2T^*; \sigma_v^2\right)$$
$$\alpha_{hw}(D) = 1 - P\left(D; \sigma_v^2\right) + P\left(D - 2T^*; \sigma_v^2\right)$$

and $\alpha_{hc} = 0$ because of no CSF. Fig. 3(d),(e) compares the model without and with partial volume effect.

C. Errors in Distance Labeling: Effect of Gray/White Manifold Location Uncertainty

The normal distance calculation is subject to error. Our approach to handling this problem is analogous to the additive error models in tomography [48]. Fig. 4 gives two examples showing how some gray matter is falsely assigned to Bank A in (a) for Brain cs2 (and, hence, interior to gray/white manifold), while some white matter falsely appears to be the right of the origin for Brain cs1 (and, hence, exterior to the gray/white manifold. See more examples in [3, Fig. 10]).

To model this error in distance labeling, we model the resulting intensity of the marked Poisson counting process as a combination of intensities from all of the underlying unobservable true distances, which contribute to the measurement location D. We define the true distance labeling process of voxel x_k as $Z(x_k)$, and model the measurements $D : (x_k) \rightarrow \mathbb{R}$ as Gaussian random variables with mean true distance $Z(x_k)$ with additive independent errors, so that the distance of each voxel

$$D(x_k) = Z(x_k) + E(x_k) \quad (16)$$

where $E(x_k)$, $k = 1, 2, \ldots$ are independent from point to point with density $p(E)$, and $Z = z$ the true normal distance to the surface coordinates. The resulting arrival intensity of the marked IDH process becomes

$$\lambda(I, D) = \int f(I; D - E) \cdot \lambda(D - E) \cdot p(E) dE. \quad (17)$$

Surface uncertainty and partial volume effects are illustrated by Fig. 3(c),(e) for exposed and hidden cortex, respectively. For the exposed cortex, the arrival rate at each measured distance is not changed by surface uncertainty effect. However, the arrival rate in the hidden cortex continuously decreases to zero after $T^\star$. In addition, this surface uncertainty also affect mean intensity values at measured distance D, the result of convolving the error function with intensity functions expected from the partial volume effect.

D. The Likelihood Function

The IDH is generated by counting the number of voxels of some image intensity at a particular set distance

$$N_{ij} = \sum_{x_k \in X} 1_{\Delta_i, \delta_j} \left(I(x_k), D(x_k)\right) \quad (18)$$

where 1 is an indicator function, $i = 0, 1, \ldots, v_{max}$. v_{max} is the maximum voxel value and $\delta_j = (j - (\delta/2), j + (\delta/2))$ marking the normal distance over some interval within the range $[min, max]$ relative to the surface coordinates. The marginal sums of the IDH along each dimension are easy to interpret. The sum over i

$$N_j = \sum_i N_{ij} \quad (19)$$

is just the number of voxels observed at a given distance from the gray/white boundary, while

$$N_i = \sum_j N_{ij} \quad (20)$$

reduces to the conventional intensity histogram.

The arrival rate of the finitely binned IDH Λ_{ij} corresponds to the number of voxel in each bin for $I \in \Delta_i$, $D \in \delta_j$, as

$$\Lambda_{ij} = \int_{\Delta_i} \int_{\delta_j} \lambda(I, D) dI dD. \quad (21)$$

From our probability model and the observed data, we can compute the log likelihood ℓ for any particular observed histogram, N_{ij} as

$$\ell = \sum_i \sum_j -\Lambda_{ij} + N_{ij} \ln(\Lambda_{ij}) \tag{22}$$

plus a constant term independent of the parameters. We assume that the cortical thickness parameters T_A and T_B differ from Bank A to Bank B. We encode this information by adding to the likelihood function the prior density which couples the parameters. Assume that T_B is Gaussian with mean T_A and standard deviation on the order of 1 mm. Then the resulting posterior distribution takes the form $\ell(\Lambda) + (1/2\sigma^2)(T_B - T_A)^2$.

E. Optimization: Maximizing Likelihood Function

We estimate all parameters in the model by maximizing the log-likelihood Function of (22). The likelihood function is shown in the previous section.

Single-Thickness Model: First, we consider $T_A = T_B = T$. The Poisson processes for the exposed cortex and the hidden cortex are independent at each bin, then the arrival rate (Λ_{ij}) is a mixture of the exposed and hidden cortex arrival rates, is Poisson distributed with the parameter equal to the sum of arrival rates at the same bin $\Lambda_{ij} = \Lambda^x_{ij} + \Lambda^h_{ij}$. Define h as the fraction of the hidden cortex $h = N^h/N$, then the parameters involved in the log-likelihood function are h, μ_c, μ_g, μ_w and σ_c, σ_g, σ_w (means and standard deviations for tissues, which are useful for segmentation), T (the thickness of both bank A and bank B), σ_v and σ_u (effects of partial volume and surface uncertainty), as well as the slope s modeling the nonuniformity of the CSF sheet.

This model is simpler than the more general double-thickness model discussed next, but has the advantage of having fewer parameters to estimate. In general, we believe this model has limited applicability, other than in some locations, where, for biological reasons, we might expect the cortex to have the same thickness on both sides of a region of CSF. One circumstance where this might take place is when there are paired structures such as those on either side of the central sulcus and we are *not* interested in (typically small) laterality differences.

Double-Thickness Model: Assume two banks A and B with different thicknesses T_A and T_B. The arrival rate Λ_{ij} of the IDH is the sum of arrival rates. In addition to T_A and T_B, three more parameters are taken into account, the fraction p of the total number of IDH voxels coming from bank A, and the fractions h_A, h_B of hidden cortex in bank A and bank B, respectively.

For computational conditioning of the initial estimates, the log-likelihood maximization procedure is evaluated in two steps. First, we use a least square approach to estimate $\mu(D)$, the mixed mean intensity value at distance D, by finding the best fit of the mean parameters μ_c, μ_g, μ_w (see the Appendix). Second, the least square estimator values for μ_c, μ_g, μ_w are used as initial condition for finding the local maxima of (22) by the Nelder-Mead simplex method [49] to estimate all the other parameters for the model. In the single-thickness model, the parameter set θ is

$$\theta = \{T, h, \mu_c, \mu_g, \mu_w, \sigma_c, \sigma_g, \sigma_w, \sigma_v, \sigma_u, s\}.$$

Similarly, the parameter set for the double-thickness model is as follows:

$$\theta = \{T_A, T_B, p, h_A, h_B, \mu_c, \mu_g, \mu_w, \sigma_c, \sigma_g, \sigma_w, \sigma_v, \sigma_u, s\}.$$

We maximize ℓ in (22) over θ by the simplex method [49].

IV. Results

To illustrate the use of our models, we computed IDHs for the left and right posterior cingulate of 10 young healthy adults (see details in [2], resolution: 0.5 mm $\times$ 0.5 mm $\times$ 0.5 mm) using the single-thickness model, which runs approximately 30 minutes for each dataset with average 80 000 voxels. We follow the reference [2] to define the boundary of posterior cingulate. Also, we studied the anterior and posterior banks of the left and right central sulcus in six subjects (healthy adults, resolution: 1 mm $\times$ 1 mm $\times$ 1 mm) under the double-thickness model, which takes approximately 10 min for each dataset with average 15 000 voxels. Delineation of the central sulcus is made on the gray/white surface. The precentral and postcentral gyri are tracked by dynamic programming [44] then the submanifold within this close path is extracted from the initial manifold, which depicted in Fig. 2.

A. Necessity of Each Component in Double-Thickness Model

The utility of any model depends on its ability to account for observed data and its ability to make predictions. As a beginning, we start with one example of the left central sulcus from cs1 (see Fig. 7) and examine the importance of each component in the model and how each component affects the model fit.

Fig. 5(a) gives representative fits of our model to the IDH for the central sulcus data in four different ways, examining the IDH (column 1), the fitted IDH (column 2), conventional intensity histogram (column 3), the distance histogram (column 4), and the mean intensity curve (column 5). The top row (a) shows the fits from the full model. Panel 2 shows the closest model fit Λ_{ij} to the measured IDH (panel 1). Column 3 shows the conventional histogram of counts versus intensity, the measured intensity histogram (black line) and the fitted intensity histogram (red line). Column 4 shows the voxel arrival rate versus set distance. Column 5 shows the mean value of the histogram versus distance. Superimposed are the model predictions showing the fits for each of these observations (red).

Each of the successive rows in Fig. 5 depicts the effects of each part in the model. Row (b) shows the results of removing partial volume effect by reducing $\sigma_v = 0.39$ mm to $\sigma_v = 0.01$ mm, which causes Λ_{ij} in Fig. 5(b) to show three more distinct clusters representing each distinct tissue type white matter, gray matter, and CSF. The observed image intensity histogram shows the biggest deviation from the predicted one at the region expected: there are more voxels with values intermediate between gray and white than expected.

Row (c) in Fig. 5 shows the results of removing the surface uncertainty effect by reducing σ_u from 0.41to 0.01 mm. Here, the gray matter abruptly ends at $D = T^\star = 2.30$ mm in the distance histogram for the hidden cortex; as well the predicted arrival rate histogram deviates from the measured one at $D = T^\star = 2.30$ mm. The discontinuities in the predicted IDH

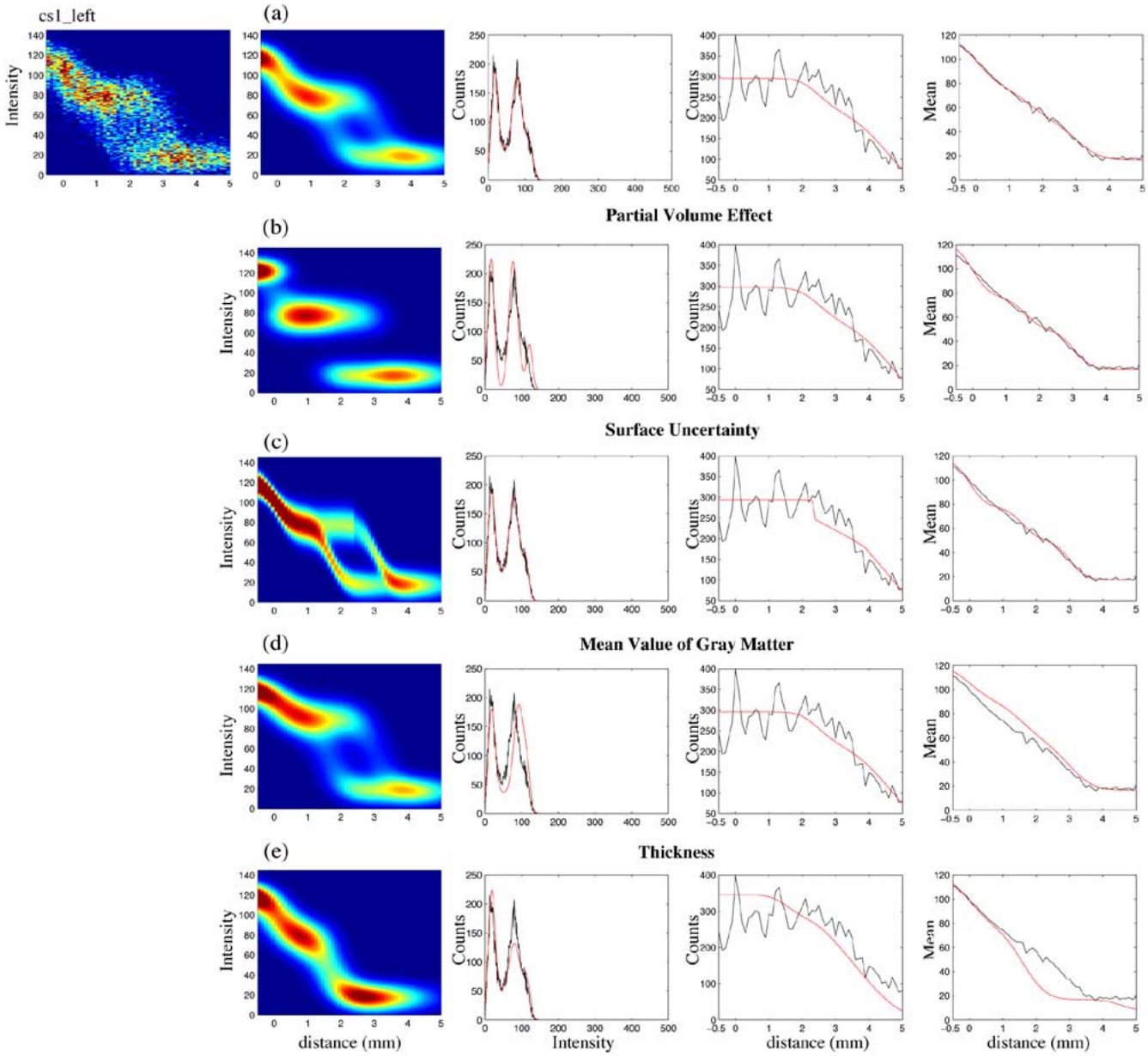

Fig. 5. Model fit for central sulcus. Row 1 shows the optimal fits for the left central sulcus of cs1 as shown in Fig. 7. Row 2 shows the voxel point-spread kernel $\sigma_v = 0.01$. Row 3 shows the surface uncertainty effect $\sigma_u = 0.01$. Row 4 shows the mean value of gray matter μ_g changed from 76.8 to 90. Row 5 shows $T_A = T_B$ for a single model of the exposed and hidden cortex mixture. Columns 1–5 show the measured IDH, fitted IDH Λ_{ij}, intensity histogram, distance histogram, and mean curve, respectively. The measured and fitted IDHs are plotted using identical color scale.

result from assuming that the banks of the two gyri have different thickness.

Row (d) in Fig. 5 illustrates how the intensity histogram and mean curve change when the mean value of gray matter shifts from $\mu_g = 76.8$ to $\mu_g = 90$. The intensity histogram and the mean curve change significantly.

Row (e) in Fig. 5 shows the dependence on a single-thickness model rather than a double-thickness model, accomplished by forcing $T_A = T_B = 1.59$ mm. The IDH no longer reflects the different thickness of the two banks of the sulcus. This reduction results in more drastic deviations between observed and expected values. Several segments of the arrival rate and image intensity histograms do not fit, and the mean intensity value as a function of distance is also poorly fitted.

B. Goodness of Fits

Fig. 6 gives representative fits for the posterior cingulate using the single-thickness model depicted by five different measures of comparison, including the IDH (columns 1,2), conventional image intensity histogram (column 3), count-rate versus distance histogram (column 4), mean image intensity versus distance (column 5), and fractional tissue contribution as a function of distance (column 6). Columns 1 and 2 compare the measured IDH and the predicted IDH of Λ_{ij} given by optimal fitting. For each subvolume the parameters of the model were found using the maximization procedure described in the Methods section. Each row corresponds to a different cortical subvolume taken from data analyzed in the laboratory of Dr. John Csernansky. Column 3 shows the conventional

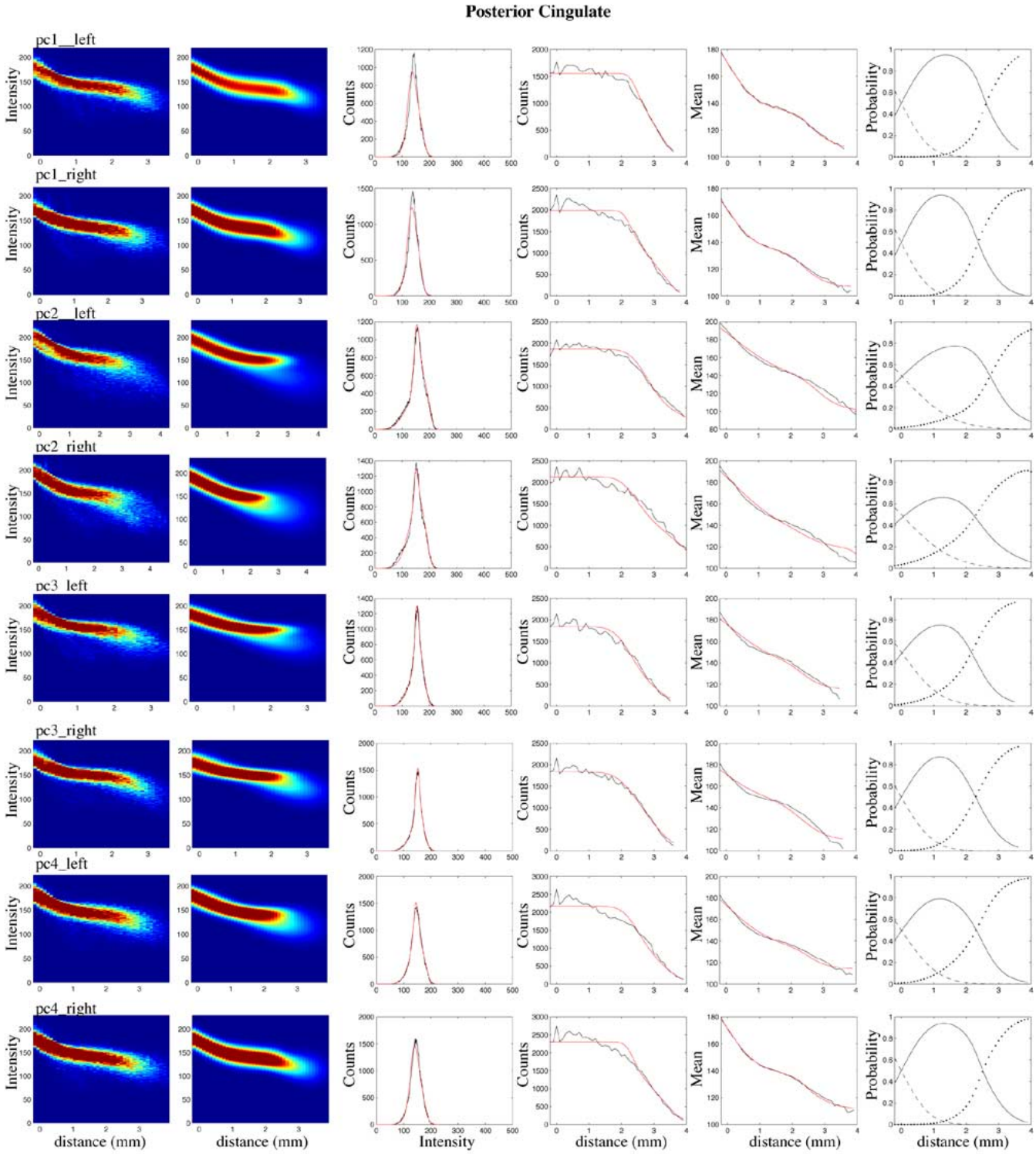

Fig. 6. Optimal fits of single-thickness model to posterior cingulates. Columns 1–5 show measured IDH, fitted IDH, intensity histogram, distance histogram, and mean curve from left to right respectively. Black lines depict the measured data; red lines depict the fitted curves of the model. Column 6 dashed, solid and dotted lines represent the fractions of white, gray, and CSF at each particular distance, respectively. Measured and fitted IDH are plotted using identical color scale.

histogram of count rates versus intensity value. Superimposed over the data are the good fit of the model. Column 4 shows the count rate versus distance with the dashed line given by the model. Column 5 shows the mean image value intensity versus distance. Column 6 shows the probability of each of the three tissue compartments as a function of distance D from the local coordinate system. At distance zero (the location of gray/white isosurface) the dashed and solid lines representing white and gray matter, intersect approximately at the probability 0.5, indicating the partial volume effect of a half white matter and half gray matter.

Fig. 7 depicts the central sulcus data using the double-thickness model. Fitting the IDH for the central sulcus is more complex because it clearly has two separate banks with clearly

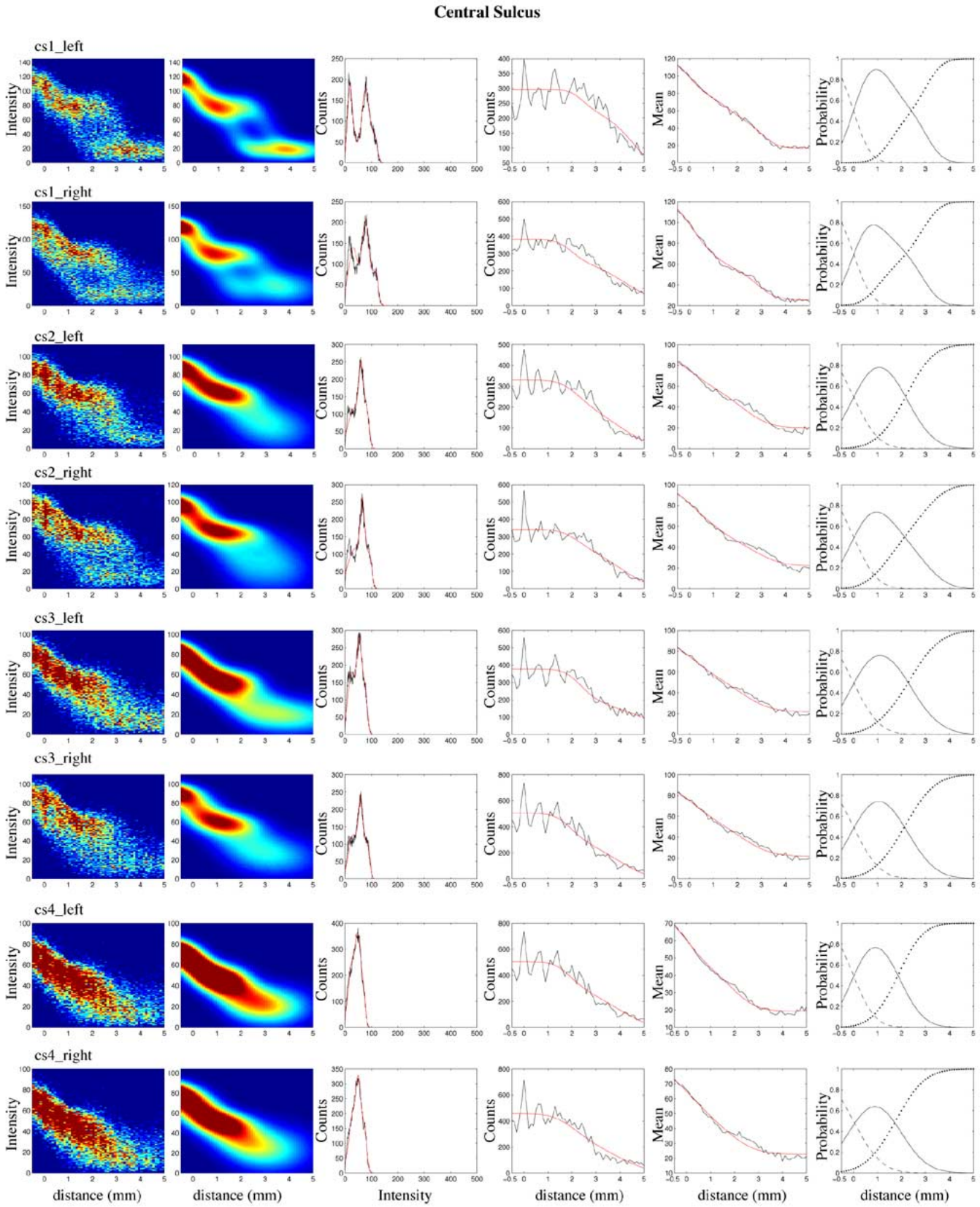

Fig. 7. Optimal fits of double-thickness model to the anterior and posterior banks of the central sulcus. Columns 1–5 show measured IDH, fitted IDH, intensity histogram, distance histogram, and mean curve from left to right, respectively. Black lines depict the measured data; red lines depict the fitted curves of the model. Column 6 dashed, solid and dotted lines represent the fractions of white, gray, and CSF at each particular distance, respectively. Measured and fitted IDH are plotted using identical color scale.

different thickness values (von Economo [42]). However, the single thickness model appears reasonable for cingulate data, perhaps because there these data involve apposition of tissue from the same Brodman's area (albeit from opposite sides of

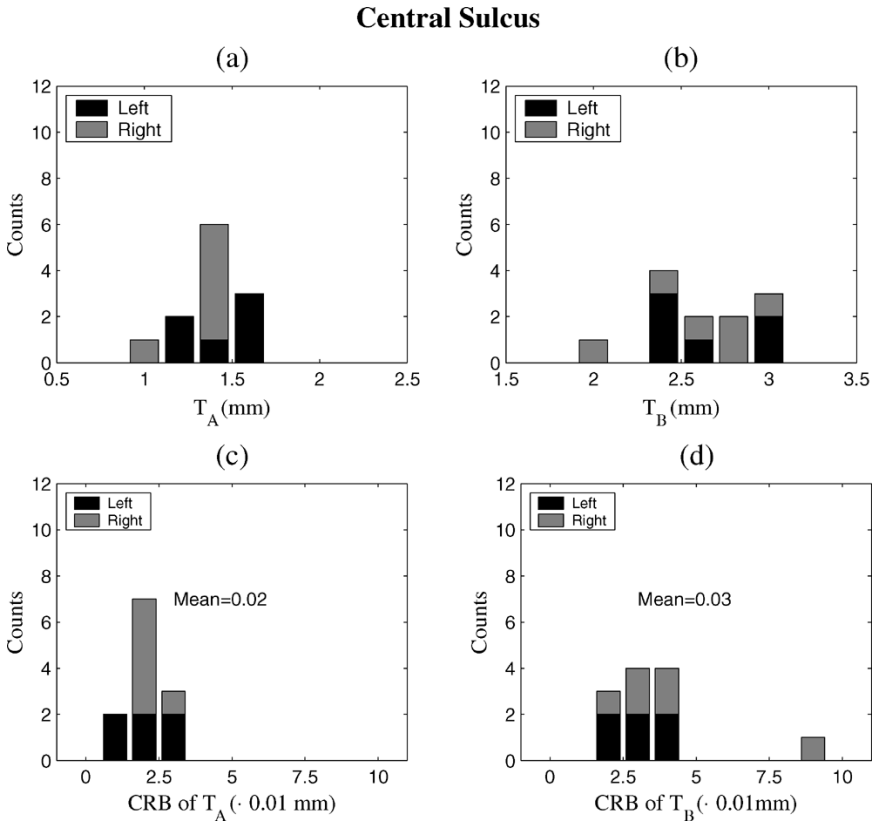

Fig. 8. Distributions of thicknesses and square root of their Cramer-Rao bounds for the central sulcus data. (a) T_A distribution. (b) T_B distribution. (c) Distribution of square root of Cramer-Rao bound of T_A. (d) Distribution of square root of Cramer-Rao bound of T_B.

the brain). Comparing the measured IDHs between the central sulcus and posterior cingulate, the IDHs (compare column 1 of Fig. 7 to column 1 of Fig. 6) clearly show that the intensity drops from the intensity of the gray matter to CSF at two distinct distances ($T_A \approx 1$ mm, $T_B \approx 2.5$ mm) signaling the cortical thicknesses for the anterior and posterior banks of the central sulcus. The same characteristics were not demonstrated in the posterior cingulate in the sense that $T_A \approx T_B$ (see Fig. 6).

C. Cramer-Rao Bound on the Thickness Estimation Accuracy

Maximum likelihood estimates are unbiased and achieve the Cramer-Rao bound, the lower bound of the variance of any unbiased estimator. The Cramer-Rao bound quantitatively estimates the accuracy of the cortical thickness estimation [50], [51]. For Poisson processes, the covariance of the estimates $\hat{\theta}_k$ and $\hat{\theta}_l$ is given by the kl entry of the matrix $I^{-1}(\theta_0)$, where $I(\theta)$ is the matrix with kl component

$$-E\left[\frac{\partial^2 \ell}{\partial\theta_k \partial\theta_l}\right] = \sum_{i,j} \frac{1}{\Lambda_{ij}} \frac{\partial \Lambda_{ij}}{\partial \theta_k} \frac{\partial \Lambda_{ij}}{\partial \theta_l}$$

where ℓ is the likelihood function in (22) and Λ_{ij} is the arrival rate at each bin of the IDH.

Fig. 8 gives distributions of the cortical thicknesses for two banks of the central sulcus (T_A and T_B) and square root of their Cramer-Rao bounds. T_A and T_B are asymptotically distributed by Gaussian with means $\hat{T}_A$ and $\hat{T}_B$, and the standard deviation on the order of 0.01 mm. The sampling distribution of T_A and T_B are highly concentrated about the true cortical thickness values.

The Cramer-Rao bound decreases with the number of samples. The original IDH has total number of voxels 13 261 with voxel size 1 mm $\times$ 1 mm $\times$ 1 mm. Considering the continuum of the cortex, we randomly down sampled the measured IDH by sampling rate 2, 4, 8 at each distance [see Fig. 9(a)], whereas the fitted IDHs for downsampled IDH are shown in Fig. 9(b). The total number of voxels in the IDHs are 13261, 6643, 3321, and 1664 from the left to right in Fig. 9(a), respectively. As shown in Fig. 9(c), the model cannot distinguish the two banks of the central sulcus at an 8 $\times$ downsampling rate, which there are just 1664 voxels on the IDH. Moreover, the square roots of Cramer-Rao bounds for T_A and T_B increase by the factor of the downsampling rate. For example, the square root of Cramer-Rao bound of T_A is 0.013 mm without downsampling, whereas 0.018 mm ($\approx \sqrt{2} \times 0.013$) at a downsampling rate 2, 0.027 mm ($\approx \sqrt{4} \times 0.013$) at a downsampling rate 4. When the IDH loses the geometric structure of the central sulcus with downsampling, the square roots of Cramer-Rao bounds of T_A, T_B become order of 1 mm implying that the estimators of T_A, T_B are no longer reliable [see Fig. 9(d)].

V. Discussion

Recent anatomical MRI studies on the human brain have been focused on the human cerebral cortex, which is a highly folded sheet of gray matter. Cortical thickness varies between 1.3 and 4.5 mm in the various parts of the brain, with an

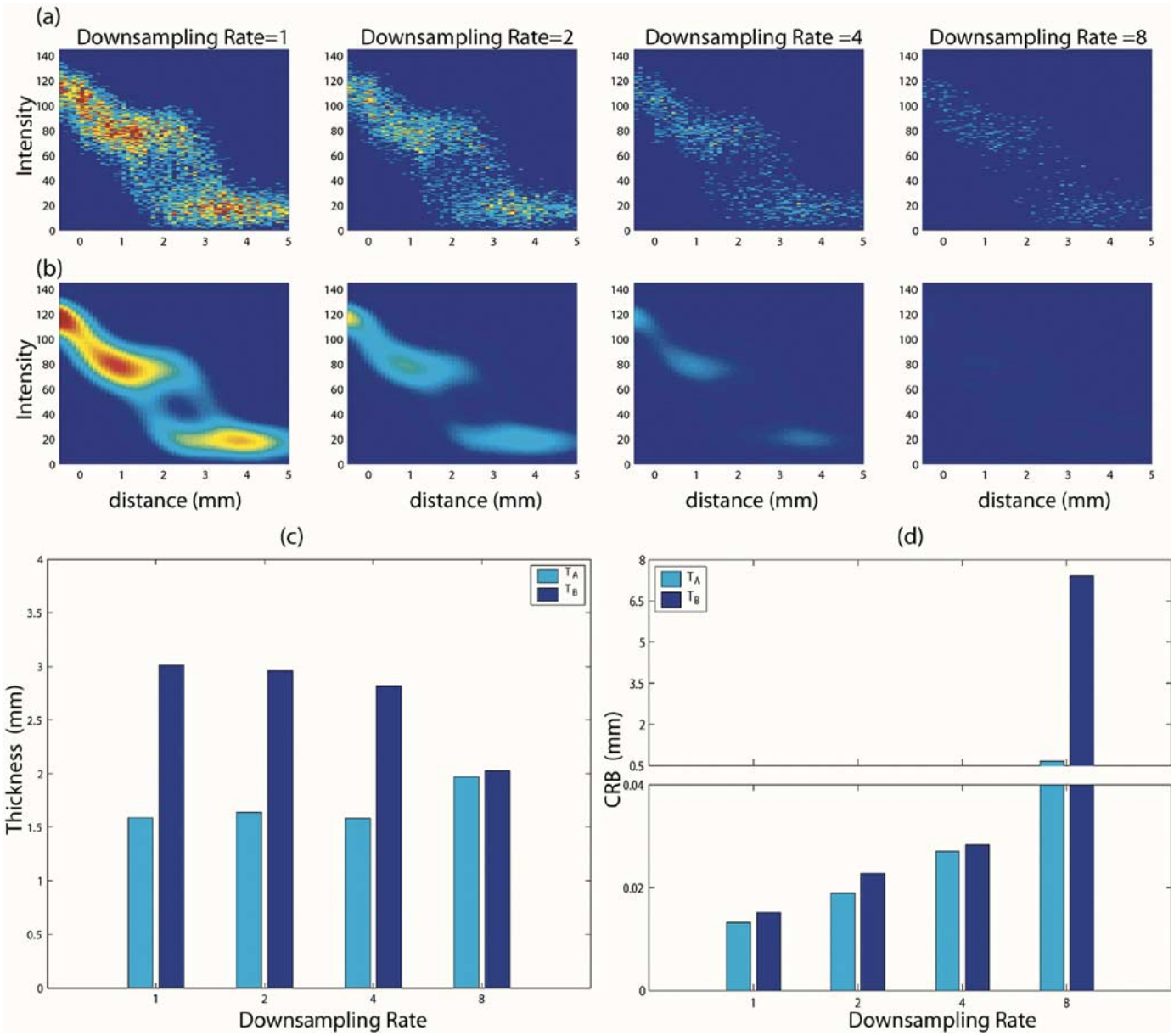

Fig. 9. Cramer-Rao bound of the left central sulcus of cs1, a function of sample rate. (a) Original IDH and the randomly downsampled IDH. (b) Fitted IDH. (c) T_A, T_B versus downsampling rate. (d) Square root of Cramer-Rao bounds of T_A, T_B versus downsampling rate. The measured and fitted IDH are plotted using identical color scale.

overall average of about 2.5 mm [42], [52], [53]. Cortical measurement has been of particular interest from the point of view of normal anatomical development as well as a wide variety of neurodegenerative and psychiatric disorders, such as aging, Alzheimer's disease and other dementias, Huntington's disease, sclerosis, and schizophrenia [2], [32]–[38], [54]. Manual methods for the cortical thickness measurement from MRI images are labor intensive, which can take a trained anatomist several days to complete. Moreover, these methods are actually able to measure the cortical volume, not cortical thickness, because the cortical thickness is a property that can only be properly measured if the location and orientation of the gray/white (interior) and gray-CSF (exterior) surfaces both are known [55].

Automated methods for cortical thickness extraction have appeared in many groups, including those of MacDonald and Evans, Dale and Fischl, Prince, Thompson, and Duncan [9], [11], [13], [54], [56], [57]. These approaches are based on the explicit manipulation of the second manifold representing the exterior surface at the gray matter transition. This presents a significant challenge since the extraction of an accurate representation of the exterior surface from MRI data is extremely difficult. The close opposition of adjacent gyri coupled to the partial volume effects of the finiteness of MRI resolution results in significant loss of resolution in the hidden regions of cortex. One of solutions to this challenge includes the approach of Magnotta *et al.* [58] to erode of the gray matter in a consistent fashion which opens up the sulci, and Jones [41] to find deep sulci for estimating the location of the exterior surface. Accurate extraction of the exterior surface in deep sulci still remains a major difficulty.

The approach presented here is to construct a stochastic model of the intensity distance histogram or IDH, relative to the local coordinates of the gray/white manifold. Such a model

allows for the direct quantification of the laminar cortex model parameters including tissue compartment values and thickness parameters of the cortical regions directly in terms of the measured IDH. In the central sulcus, our estimates for T_A and T_B are in line with von Economo, as are our estimates for T in the cingulate gyrus. The Cramer-Rao bounds on these estimates are small compared with our estimates, at least within the range of samples which have nearly 2000 voxels. The power of such an explicit stochastic model in terms of geometric parameters directly is that accurate estimation of the cortical thicknesses of cortical banks can be obtained without any explicit geometric representation of the transition region associated with the change from gray matter to CSF in the laminar model. The exterior manifold is never directly estimated. Since methods dependent on the explicit acquisition of the exterior manifold will result directly in extra variance in the estimation of the cortical thickness, the proposed method which calculates the laminar thickness via implicit manipulation of the structural change from gray to CSF offers a significant opportunity for increased power for the accurate estimation of laminar geometry.

We have not explicitly allowed for the influence of curvature in this model, which intuitively affects the arrival rate at each distance and implies that the arrival rate is not constant over the surface. The arrival rate tends to increases on the location with positive curvature, while the arrival rate decreases on those with negative curvature. The uniform distribution assumption of the arrival rate may cause overestimation of the cortical thickness in the sulcus region and underestimation in the gyrus region. We also acknowledge that although we model local portions of cortex as a homogeneous sheet with a fixed thickness T, in fact T slowly varies over this region. Our current model give the mean estimate of the cortical thickness. Of course, this fixed T approximation is most likely to be appropriate over small cortical regions rather than larger ones. However, estimates of such parameters as the statistics of gray matter, white matter and CSF image values are likely to be improved by incorporating more, rather than less tissue, so the issue of the extent of the cortical region in our model for which our estimate is optimal in some sense remains an open question.

Other future efforts will focus on study of such variability. Our definition of T^* may occasionally lead to errors in assigning voxels to the correct bank when there is a thin strip of CSF separating two banks of cortex with large differences in thickness. We believe that this effect is minimal for the anatomical structures studied here primarily because the regions tend to be near regions of high positive curvature (gyral crowns) and believe that the majority of voxels in exposed cortex are properly associated, leading to only small errors given the size of the structures we discuss here. Of course, as one would analyze smaller and smaller cortical regions, the effect of this error would grow larger, and we believe that our model must be extended in the future to handle this problem, perhaps by using a more sophisticated rule for assigning voxels to a sulcal bank.

We also plan future efforts relating to the validity and reliability of our model. In general, we believe the results we report here are reasonably close to those reported by others, especially considering the number of computations and assumptions necessary to both our model and those of others. Because of the variability of the cortex and its convoluted shape, finding a gold standard for validity is difficult. However, it would certainly be possible to cross-validate our results against those reported by others if the same data sets were analyzed, and we believe such studies are likely to improve our understanding of exactly what the key assumptions of our model are, and where they may break down.

The presented model can be used for a variety of studies, especially in the pathological study. We are conducting studies in a number of diseases, including Alzheimer's and schizophrenia, and look forward to reporting on pathological changes in cortical thickness in the near future. In addition, we intend to improve segmentation based on this model, which incorporates intensity and distance properties of MRI voxels, instead of traditional segmentation approaches based on just intensity information. The model can be trivially extended to estimating surface area via the laminar approximation. In addition, an extension of the model to handle curvature and variable cortical thickness more accurately might also yield estimates of these parameters, which might have biological significance.

APPENDIX
LEAST SQUARE ESTIMATION OF MEANS

Without the effect of surface uncertainty, a mixed mean at a true distance $\mu(Z)$ is a linear combination of mean values $\mu_x(Z)$, $\mu_h(Z)$ of the exposed (10) and hidden cortex (14) as the form

$$\mu(Z) = p_1(Z) \cdot \mu_x(Z) + p_2(Z) \cdot \mu_h(Z) \tag{23}$$

where $p_1(Z) = 1_{\leq T^*}(Z) \cdot h_1 + 1_{>T^*}(Z)$ and $p_2(Z) = 1_{\leq T^*}(Z) \cdot (1 - h_1)$ are the fractions of exposed and hidden cortex at each true distance Z. Assume $U(Z)$ is the vector

$$U(Z) = \begin{pmatrix} \mu(Z_1) \\ \mu(Z_2) \\ \vdots \\ \mu(Z_n) \end{pmatrix}$$

and A(Z) is the $n \times n$ matrix of the form shown in the equation at the bottom of the page, where all αs are given in Section III-B. Equation (23) is written in the matrix form as

$$U(Z) = A(Z) \cdot \begin{pmatrix} \mu_c \\ \mu_g \\ \mu_w \end{pmatrix}.$$

$$A(Z) = \begin{pmatrix} p_1 \cdot \alpha_{xc}(Z_1) & p_1 \cdot \alpha_{xg}(Z_1) + p_2 \cdot \alpha_{hg}(Z_1) & p_1 \cdot \alpha_{xw}(Z_1) + p_2 \cdot \alpha_{hw}(Z_1) \\ p_1 \cdot \alpha_{xc}(Z_2) & p_1 \cdot \alpha_{xg}(Z_2) + p_2 \cdot \alpha_{hg}(Z_2) & p_1 \cdot \alpha_{xw}(Z_2) + p_2 \cdot \alpha_{hw}(Z_2) \\ \vdots & \vdots & \vdots \\ p_1 \cdot \alpha_{xc}(Z_n) & p_1 \cdot \alpha_{xg}(Z_n) + p_2 \cdot \alpha_{hg}(Z_n) & p_1 \cdot \alpha_{xw}(Z_n) + p_2 \cdot \alpha_{hw}(Z_n) \end{pmatrix}$$

With the surface uncertainty effect, the mixed mean at a measured distance D is the convolution result of $\mu(Z)$ with kernel $p(E)$, giving

$$U(D) = \left(\int A(D-E) \cdot p(E) dE \right) \cdot \begin{pmatrix} \mu_c \\ \mu_g \\ \mu_w \end{pmatrix}$$

which are linear equations with respect to μ_c, μ_g, and μ_w and solved by the least-squares method.

ACKNOWLEDGMENT

The authors would like to thank Dr. J. T. Ratnanather for his contributions.

REFERENCES

[1] B. A. Wandell, *Foundations of Vision*. Sunderland, MA: Sinauer, 1995.

[2] M. I. Miller, M. Hosakere, A. R. Barker, C. E. Priebe, N. Lee, J. T. Ratnanather, L. Wang, M. Gado, J. C. Morris, and J. G. Csernansky, "Labeled cortical mantle distance maps of the cingulate quantify differences between dementia of the Alzheimer type and healthy aging," *Proc. Natl. Acad. Sci*, vol. 100, pp. 15172–15 177, 2003.

[3] M. I. Miller, A. B. Massie, J. T. Ratnanather, K. N. Botteron, and J. G. Csernansky, "Bayesian construction of geometrically based cortical thickness metrics," *NeuroImage*, vol. 12, pp. 676–687, 2000.

[4] J. T. Ratnanather, K. N. Botteron, T. Nishino, A. B. Massie, R. M. Lal, and S. G. Patel, "Validating cortical surface analysis of medial prefrontal cortex," *NeuroImage*, vol. 14, pp. 1058–1069, 2001.

[5] A. M. Dale and M. I. Sereno, "Improved localization of cortical activity by combining EEG and MEG with MRI cortical surface reconstruction: a linear approach," *J. Cognitive Neurosci.*, vol. 5, no. 2, pp. 162–176, 1993.

[6] W. M. Wells III, W. E. L. Grimson, R. Kikinis, and F. A. Jolesz, "Adaptive segmentation of MRI data," *IEEE Trans. Med. Imag.*, vol. 15, no. 4, p. 429, Aug. 1996.

[7] T. Kapur, W. Grimson, W. M. Wells III, and R. Kikinis, "Segmentation of brain tissue from magnetic resonance images," *Med. Image Anal.*, vol. 1, pp. 109–127, 1996.

[8] P. M. Thompson, C. Schwartz, and A. W. Toga, "High-resolution random mesh algorithms for creating a probabilistic 3-D surface atlas of the human brain," *NeuroImage*, vol. 3, no. 1, pp. 19–34, 1996.

[9] A. M. Dale, B. Fischl, and M. I. Sereno, "Cortical surface-based analysis I: segmentation and surface reconstruction," *NeuroImage*, vol. 9, pp. 179–194, 1999.

[10] M. Joshi, J. Cui, K. Doolittle, S. Joshi, D. Van Essen, L. Wang, and M. I. Miller, "Brain segmentation and the generation of cortical surfaces," *NeuroImage*, vol. 9, pp. 461–476, 1999.

[11] C. Xu, D. L. Pham, M. E. Rettmann, D. N. Yu, and J. Prince, "Reconstruction of the human cerebral cortex from magnetic resonance images," *IEEE Trans. Med. Imag.*, vol. 18, no. 6, pp. 467–479, Jun. 1999.

[12] G. Harris, N. C. Andreasen, T. Cizadlo, J. M. Bailey, H. J. Bockholt, V. A. Magnotta, and S. Arndt, "Improving tissue classification in MRI: a three-dimensional multispectral discriminant analysis method with automated training class selection," *J. Comput. Assist. Tomogr.*, vol. 23, no. 1, pp. 144–154, 1999.

[13] D. MacDonald, N. Kabani, D. Avis, and A. C. Evans, "Automated 3-D extraction of inner and outer surfaces of cerebral cortex from MRI," *NeuroImage*, vol. 12, pp. 340–356, 2000.

[14] B. Fischl, A. Liu, and A. M. Dale, "Automated manifold surgery: constructing geometrically accurate and topologically correct models of the human cerebral cortex," *IEEE Trans. Med. Imag.*, vol. 20, no. 1, pp. 70–80, Jan. 2001.

[15] Y. Zhang, M. Brady, and S. Smith, "A hidden Markov random field model for segmentation of brain MR images," *Proc. SPIE Med. Imag.*, pp. 1126–1137, 2000.

[16] ——, "Segmentation of brain MR images through a hidden Markov random field model and the expectation maximization algorithm," *IEEE Trans. Med. Imag.*, vol. 20, no. 1, pp. 45–57, Jan. 2001.

[17] ——, "A statistical framework for automatic brain MR image segmentation," *NeuroImage*, vol. 13, no. 6, p. S291, 2001.

[18] D. W. Shattuck, S. R. Sandor-Leahy, K. A. Schaper, D. A. Rottenberg, and R. Leahy, "Magnetic resonance image tissue classification using a partial volume model," *NeuroImage*, vol. 13, no. 5, pp. 856–876, 2001.

[19] B. Fischl, D. H. Salat, E. Busa, M. Albert, M. Dieterich, C. Haselgrove, A. van der Kouwe, R. Killiany, D. Kennedy, S. Klaveness, A. Montillo, N. Makris, B. Rosen, and A. M. Dale, "Whole brain segmentation: automated labeling of neuroanatomical structures in the human brain," *Neuron*, vol. 33, pp. 341–355, 2002.

[20] X. Han, C. Xu, D. Tosun, and J. L. Prince, "Cortical surface reconstruction using a topology preserving geometric deformable model," in *Proc. Workshop Mathemat. Meth. Biomed. Image Anal.*, Kauai, HI, Dec. 2001, pp. 213–220.

[21] X. Han, C. Xu, U. Braga-Neto, and J. Prince, "Topology correction in brain cortex segmentation using a multiscale, graph-based algorithm," *IEEE Trans. Med. Imag.*, vol. 21, no. 2, pp. 109–121, Feb. 2002.

[22] D. W. Shattuck and R. M. Leahy, "Automated graph-based analysis and correction of cortical volume topology," *IEEE Trans. Med. Imag.*, vol. 20, no. , pp. 1167–1177, 2001.

[23] S. Joshi, J. Wang, M. I. Miller, D. C. Van Essen, and U. Grenander, "On the differential geometry of the cortical surface," in *Vision Geometry IV, Proc. SPIE 1995 Int. Symp. Opt. Sci., Eng., and Instrument.*, vol. Vol. 2573, San Diego, CA, Aug. 1995, pp. 304–311.

[24] D. C. Van Essen, H. A. Drury, S. Joshi, and M. I. Miller, "Functional and structural mapping of human cerebral cortex: solutions are in the surfaces," *Proc. Nat. Acad. Sci*, vol. 95, pp. 788–795, 1998.

[25] A. W. Toga, *Brain Warping*. London, U.K.: Academic, 1999, ch. 19, pp. 337–363.

[26] S. Angenent, S. Haker, A. Tannenbaum, and R. Kikinis, "On the Laplace-Beltrami operator and brain surface flattening," *IEEE Trans. Med. Imag.*, vol. 18, no. 8, pp. 700–711, Aug. 1999.

[27] B. Fischl, M. I. Sereno, and A. M. Dale, "Cortical surface-based analysis II: inflation, flattening, and a surface-based coordinate system," *NeuroImage*, vol. 9, pp. 195–207, 1999.

[28] B. Fischl, M. I. Sereno, R. B. H. Tootell, and A. M. Dale, "High-resolution inter-subject averaging and a surface-based coordinate system," *Hum. Brain Map.*, vol. 8, pp. 272–284, 1999.

[29] M. K. Hurdal, P. L. Bowers, K. Stephenson, D. L. Sumners, K. Rehm, K. Schaper, and D. A. Rottenberg, "Quasiconformally flat mapping the human cerebellum," in *Lecture Notes in Computer Science*, C. Taylor and A. Colchester, Eds. Berlin, Germany: Springer-Verlag, 1999, pp. 279–286.

[30] J. W. Lewis and D. C. Van Essen, "Mapping of architectonic subdivisions in the macaque monkey, with emphasis on parieto-occipital cortex," *J. Comp. Neurol.*, vol. 428, pp. 79–111, 2000.

[31] C. R. Collins and K. Stephenson, "A circle packing algorithm," *Comput. Geom. Theory Applicat.*, vol. 25, pp. 233–256, 2003.

[32] M. J. DeLeon, A. E. George, J. Golomb, C. Tarshish, A. Convit, and A. Kluger *et al.*, "Frequency of hippocampal formation atrophy in normal aging and Alzheimer's disease," *Neurobiol. Aging*, vol. 18, pp. 1–11, 1997.

[33] C. R. Jack Jr, R. C. Petersen, Y. C. Xu, S. C. Waring, P. C. O'Brien, E. Tangalos, G. E. Smith, R. J. Ivnik, and E. Kokmen, "Medial temporal atrophy on MRI in normal aging and very mild Alzheimer's disease," *Neurology*, vol. 49, pp. 786–790, 1997.

[34] J. C. Morris, "Is Alzheimer's disease inevitable with age?: lessons from clinicopathologic studies of healthy aging and very mild alzheimer's disease," *J. Clin. Invest.*, vol. 104, pp. 1171–1173, 1999.

[35] M. S. Albert, "Cognitive and neurobiologic markers of early Alzheimer disease," *Proc. Nat. Acad. Sci.*, vol. 93, pp. 13547–13 551, 1996.

[36] J. A. Kaye, T. Swihart, D. Howieson, A. Dame, M. M. Moore, T. Karnos, R. Camicioli, M. Ball, B. Oken, and G. Sexton, "Volume loss of the hippocampus and temporal lobe in healthy elderly persons destined to develop dementia," *Neurology*, vol. 48, pp. 1297–1304, 1997.

[37] J. P. Vonsattel and M. DiFiglia, "Huntington disease," *J Neuropath. Exp. Neurol.*, vol. 57, pp. 369–384, 1998.

[38] R. B. Zipursky, E. K. Lambe, S. Kapur, and D. J. Mikulis, "Cerebral gray matter volume deficits in first episode psychosis," *Arch. Gen. Psych.*, vol. 55, pp. 540–546, 1998.

[39] J. C. Baron, G. Chtelat, B. Desgranges, G. Perchey, B. Landeau, V. Sayette, and F. Eustache, "In vivo mapping of gray matter loss with voxel-based morphometry in mild Alzheimer's disease," *NeuroImage*, vol. 14, no. 2, pp. 298–309, 2001.

[40] C. D. Good, I. S. Johnsrude, J. Ashburner, R. N. A. Henson, K. J. Friston, and R. S. J. Frackowiak, "A voxel-based morphometric study of ageing in 465 normal adult human brains," *NeuroImage*, vol. 14, no. 1, pp. 21–36, 2001.

[41] S. E. Jones, B. R. Buchbinder, and I. Aharon, "Three-dimensional mapping of cortical thickness using Laplace's equation," *Hum. Brain Map.*, vol. 11, pp. 12–32, 2000.

[42] C. V. Economo, *The Cytoarchitectonics of the Human Cerebral Cortex*. Oxford, U.K.: Oxford Univ. Press, 1929.

[43] W. E. Lorensen and H. E. Cline, "A high resolution 3-D surface construction algorithm," *Comput. Graph.*, vol. 21, pp. 163–169, 1987.

[44] J. T. Ratnanather, P. E. Barta, N. A. Honeycutt, N. Lee, H. M. Morris, A. C. Dziorny, M. K. Hurdal, G. D. Pearlson, and M. I. Miller, "Dynamic programming generation of boundaries of local coordinatized submanifolds in the neocortex: application to the planum temporale," *NeuroImage*, vol. 20, pp. 359–377, 2003.

[45] D. L. Snyder and M. I. Miller, *Random Point Processes in Time and Space*. New York: Springer-Verlag, 1991.

[46] M. I. Miller, T. J. Schaewe, C. Bosch, and J. J. H. Ackerman, "A mathematical signal model for phase and frequency encoded magnetic resonance imaging data," *J. Magn. Reson.*, no. 107, pp. 210–222, 1995.

[47] T. J. Schaewe and M. I. Miller, "Parallel algorithms for maximum *a posterori* estimation of spin density and spin-spin decay in magnetic resonance imaging," *IEEE Trans. Med. Imag.*, vol. 14, no. 2, pp. 362–373, Jun. 1995.

[48] D. L. Snyder and D. G. Politte, "Image reconstruction from list-mode data in an emission tomography system having time of flight measurements," *IEEE Trans. Nucl. Sci.*, vol. 20, no. NS-3, pp. 1843–1849, 1983.

[49] J. C. Lagarias, J. A. Reeds, M. H. Wright, and P. E. Wright, "Convergence properties of the Nelder-Mead simplex method in low dimensions," *SIAM J. Optimization*, vol. 9, no. 1, pp. 112–147, 1998.

[50] J. A. Rice, *Mathematical Statistics and Data Analysis*. Belmont, CA: Duxbury, 1995, pp. 275–277.

[51] P. J. Bickel and K. A. Doksum, *Mathematical Statistics: Basic Ideas and Selected Topics*. San Francisco, CA: Holden-Day, 1977, pp. 129–131.

[52] K. A. Brodmann, *In Perceptual Neuroscience: The Cerebral Cortex*. Cambridge, MA: Harvard Univ. Press, 1905.

[53] K. A. Meynert, *The Cytoarchitectonics of the Human Cerebral Cortex*. Oxford, U.K.: Oxford Univ. Press, 1867.

[54] E. R. Sowell, B. S. Peterson, P. M. Thompson, S. E. Welcome, A. L. Henkenius, and A. W. Toga, "Mapping cortical change across the human life span," *Nat. Neurosci.*, vol. 6, pp. 309–315, 2003.

[55] J. R. Meyer, S. Roychowdhury, E. J. Russell, C. Callahan, D. Gitelman, and M. M. Mesulam, "Location of the central sulcus via cortical thickness of the precentral and postcentral gyri on MR," *Am. J. Neuroradiol.*, vol. 17, pp. 1699–1706, 1996.

[56] X. Zeng, L. H. Staib, R. T. Schultz, and J. S. Duncan, "Segmentation and measurement of the cortex from 3-D MR images using coupled surfaces propagation," *IEEE Trans. Med. Imag.*, vol. 18, no. 10, pp. 100–111, Oct. 1999.

[57] B. Fischl and A. M. Dale, "Measuring the thickness of the human cerebral cortex from magnetic resonance images," *Proc. Nat. Acad. Sci.*, vol. 97, no. 20, pp. 11 050–11 055, 2000.

[58] V. A. Magnotta, N. C. Andreasen, S. K. Schultz, G. Harris, T. Cizadlo, D. Heckel, P. Nopoulos, and M. Flaum, "Quantitative *in vivo* measurement of gyrification in the human brain: changes associated with aging," *Cereb. Cortex*, vol. 9, pp. 151–160, 1999.